Mon. Not. R. Astron. Soc. **378,** 482–492 (2007) doi:10.1111/j.1365-2966.2007.11765.x

Fibre modal power distributions in astronomy and their application to OH-suppression fibres

J. Corbett,★ T. Butterley and J. R. Allington-Smith
Centre for Advanced Instrumentation, Department of Physics, University of Durham, South Road, Durham DH1 3LE

Accepted 2007 March 20. Received 2007 February 16; in original form 2006 September 13

ABSTRACT

Knowledge of the modal power distribution (MPD) in multimode optical fibre is crucial for the design of OH-suppressing fibre systems based on single-mode fibre arrays. MPDs allow us to estimate the minimum number of modes required to provide good data quality for astronomy so that we can reduce the size and cost of the single-mode array. This paper shows how the MPD of multimode fibres changes when fed with the telescope point spread function and when illuminated with an image of the telescope exit pupil via a field lenslet under conditions of ideal, natural and partially corrected seeing. We show that OH-suppressing fibres operating at 800 nm require arrays of single-mode fibres that will be challenging to manufacture. The complete *J* and *H* bands, however, require as few as 40–80 modes.

Key words: atmospheric effects – instrumentation: spectrographs – techniques: spectroscopic.

1 INTRODUCTION

OH-suppressing fibres, first reported by Bland-Hawthorn, Englund & Edvell (2004), convert a multimode fibre (MMF) into an array of single-mode (SM) fibres on which can be imprinted fibre Bragg gratings. The SM array (SMA) is then re-fused into a MMF yielding a multimode fibre device capable of suppressing certain wavelengths such as the atmospheric OH lines with SM performance (Fig. 1). A working example of such a device has recently been reported by Leon-Saval et al. (2005).

In this paper we determine the distribution of power within the input multimode step index fibre (MMF) used to transport starlight in an astronomical instrument when fed (i) by the telescope point spread function (PSF) and (ii) with an image of the telescope exit pupil via a lenslet in the telescope image plane. The manufacturability of these devices is directly related to the number of cores within the SMA. The modal power distribution (MPD) is then used to predict the astronomical performance of the device as a function of the number of SM cores.

It is worth noting that, to date, the primary proposed use of these fibre devices has been in OH suppression and for this reason they are called OH-suppression fibres throughout for brevity. However, this analysis is generally applicable to any MMF–SMA–MMF-type device fed from the telescope.

2 THE FIBRE MODEL

With reference to Fig. 2, in z-invariant waveguides, such as optical fibre, each mode, n, can be expressed as

$$\boldsymbol{H}_n = (\boldsymbol{h}_{x,y} + h_z\hat{\boldsymbol{z}}) \exp(\mathrm{i}\beta z), \tag{1}$$

where β is known as the propagation constant and is defined below.

★E-mail: j.c.w.corbett@durham.ac.uk

In most commercially available optical fibre, the core and cladding refractive indices are almost identical. This is done in order to reduce the need for exotic dopents, used to lower the cladding index with respect to the core, but that subsequently increases losses via scattering. In weakly guiding fibres h_z is negligible in comparison to the transverse components $\boldsymbol{h}_{x,y} = h_x(x, y)\hat{\boldsymbol{x}} + h_y(x, y)\hat{\boldsymbol{y}}$ and the modes of the fibre are seen to be approximately, completely transverse.

Each valid mode $\boldsymbol{h}_{x,y}$ within the fibre must satisfy the equation

$$\boldsymbol{O}\boldsymbol{h}_{x,y} = \beta^2\boldsymbol{h}_{x,y}, \tag{2}$$

where $\boldsymbol{O}$ is an operator (Snyder & Love 1983) and

$$U = \rho\left(k_\mathrm{o}^2 n_\mathrm{core}^2 - \beta^2\right). \tag{3}$$

Here, ρ is the fibre core radius, n_core is the core refractive index and k_o is the free-space wavenumber magnitude.

The macroscopic state of the fibre can be described completely via the fibre parameter, V,

$$V = k_\mathrm{o} a \Theta, \tag{4}$$

where a is the fibre radius in meters, Θ is the numerical aperture and k_o is the free-space wavenumber. U and V can be used to make equation (2) dimensionless. Thence solving in the core and cladding separately and specifying that any valid modal solution must be continuous and have a continuous first derivative across the boundary yields

$$U\frac{J_{l+1}(U)}{J_l(U)} = W\frac{K_{l+1}(W)}{K_l(W)}, \tag{5}$$

where $V^2 = U^2 + W^2$ and J is the Bessel function of the first kind and K is the modified Bessel function of the second kind. Setting V, then at each value of integer $l \in [0, \infty[$, m eigenvalues, $U_m \leqslant V$,

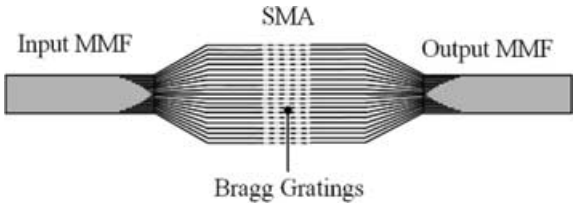

Figure 1. The input MMF transforms into the SMA on which the Bragg gratings are encoded. The reverse transition then reforms the SMA into the output MMF.

are found to satisfy equation (5). At each value of l, m, there exist four modes

$$\text{Even HE}_{l+1,m}\ \boldsymbol{h}_{tn} = CF_l(U_m)[\sin(l\phi)\hat{\boldsymbol{x}} + \cos(l\phi)\hat{\boldsymbol{y}}] \tag{6a}$$

$$\text{Odd HE}_{l+1,m}\ \boldsymbol{h}_{tn} = CF_l(U_m)[\cos(l\phi)\hat{\boldsymbol{x}} - \sin(l\phi)\hat{\boldsymbol{y}}] \tag{6b}$$

$$\text{Even EH}_{l-1,m}\ \boldsymbol{h}_{tn} = CF_l(U_m)[\sin(l\phi)\hat{\boldsymbol{x}} - \cos(l\phi)\hat{\boldsymbol{y}}] \tag{6c}$$

$$\text{Odd EH}_{l-1,m}\ \boldsymbol{h}_{tn} = CF_l(U_m)[\cos(l\phi)\hat{\boldsymbol{x}} + \sin(l\phi)\hat{\boldsymbol{y}}], \tag{6d}$$

where C is a constant, $\phi = \text{Arg}(x, y)$ is the polar angle in the x–y plane and F_l is a function of l and U_m (Snyder & Love 1983). As for all fields in this paper, the $\exp(-i\omega t)$ term is assumed, but omitted for clarity.

In the $l = 1$ case, the Even EH and Odd EH modes have a zero h_z component even when computed using a non-weakly guiding model (i.e. including h_z) and are therefore known as the TM and TE modes, respectively.

Separate non-weakly guiding equations, similar to equation (5), exist for each of the HE, EH, TE and TM modes but in the weakly guiding case of $n_{\text{core}} \approx n_{\text{cladding}}$ most typically found in practical applications these equations coincide to within a few parts in 10^5 in U, and Fig. 3(a) is a typical plot of U (V) for this case, with U_m curves for each l indistinguishable from each other.

Note from equation (4) and Fig. 3 that as a and Θ increase and λ decreases, V increases and more modes are supported, appealing to the notion that smaller wavelengths in a larger waveguide will increase the total number of supported modes.

2.1 From the MMF to the SMA

The SMA made from M, SM cores can support M modes (Leon-Saval et al. 2005) which under the assumption of a strictly adiabatic transition, are transposed into the array from the fibre in order of increasing U within the MMF, e.g. in order of HE_{11}, TE_{01}, HE_{21} (Odd + Even), TM_{01}, EH_{11} (Odd + Even), HE_{31} (Odd + Even), HE12, etc. at $V > 4.2$ in Fig. 3(a). However, the U (V) curves can sometimes be seen to cross near the cut-off region, i.e. near $U = V$ in Fig. 3(b). Fig. 3(b) was computed using the non-weakly guiding modal model; however, the much simpler weakly guiding model (presented in the previous section) is used throughout this work for simplicity and considerably reduced computation time. This introduces a small uncertainty in the results in some circumstances.

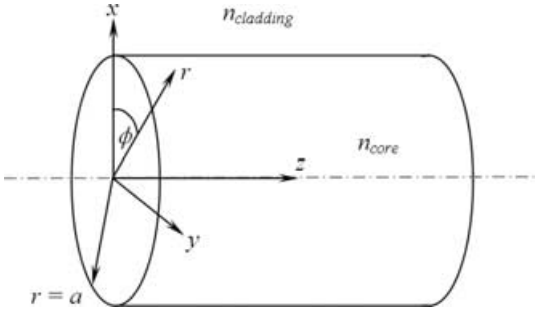

Figure 2. The fibre geometry.

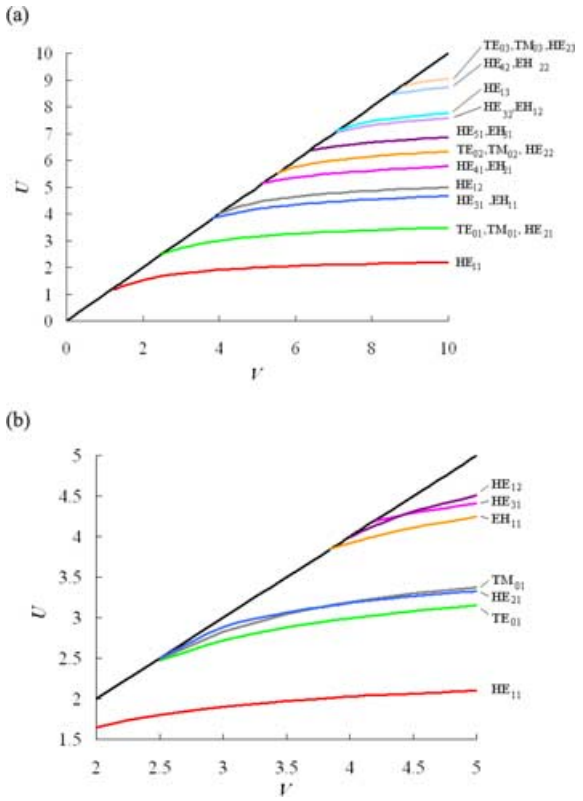

Figure 3. (a) U (V) for a weakly guiding step index fibre, (b) U (V) for step index fibre of core refractive index, $n_{\text{core}} = 2.5$ and cladding refractive index $n_{\text{cladding}} = 1.5$ chosen to amplify the crossover of some modes near to cut-off. In both cases the black line denotes $U = V$.

For example, with reference to Figs 3(a) and (b), in the scalar case, it is possible to compute the coupling efficiency into the HE_{31} and EH_{11} modes but not the HE_{21} if $V = 3.9$ (say) in the weakly guiding model. However, the non-weakly guiding, and therefore more accurate, description tells us that HE_{31} is no longer supported but the HE_{21} is at this V value. Therefore it is not strictly possible to assume that an SMA supporting M modes will couple the lowest M modes of the MMF.

However, at any given value of V only approximately 8 per cent of the supported modes are near cut-off Birks (private correspondence), hence it is safe to assume sequential transfer of weakly guiding modal indices with an uncertainty of <8 per cent or so when the number of supported or populated modes is greater than M, which does not affect the efficacy of this analysis.

2.2 The geometrical, ray optical, model

Snyder & Love (1983) show that for $U \gg 1$ each value of U can be associated with a unique characteristic ray angle, θ,

$$U = \frac{2\pi a n_{\text{core}} \sin\theta}{\lambda} = V\frac{\sin\theta}{\sin\Theta} \tag{7}$$

azimuthal with respect to the fibre axis and hence $\theta \in [0, \Theta]$. The ray optical model, whereby wavefronts are modelled using rays, is therefore approximately applicable within highly multimode optical fibre (one mode = one ray).

The commonly used formula for the number of supported (bound) MMF modes, N for a given $\theta_{\max}$, is also based on the $U \gg 1$ approximation (Pask, Snyder & Mitchell 1975) and is given by

$$N = U^2/n, \tag{8}$$

where n is an integer whose value depends on how the modes of the fibre are counted. For instance, equation (8) applies to the fully vectorial mode designation when $n = 2$. The linearly polarized (LP) modes of the fibre are the sum of all four vectorial fields at each l, m to yield the $\mathrm{LP}_{(l-1,m)}$ modes and so the number of LP modes is reduced to $N = U^2/8$. Inspecting Fig. 3(a) we see that in the $l = 0$ and 1 cases one and three vectorial mode(s), respectively, are approximately associated with a single θ but for all $l > 1$, there are two vectorial modes per θ and the number of SMA modes is well approximated by $N = U^2/4$.

Looking again at Fig. 3(a), we see that $U_{\max} \approx V$ for any V and thence replacing U with V in equation (8) yields the total supported (bound) modes within the numerical aperture of the fibre. Further, since we start with the electromagnetic field model and seek correspondence with the geometrical ray model, at $U_{\max}$, $\theta_{\max} \approx \Theta$ and the maximum supported angle within the fibre is very nearly the geometrical (ray) numerical aperture itself. The fractional error associated with equation (8) is $1/U$.

2.3 The general effect of $M < N$

In this section we investigate, in general terms, the effect of there being fewer supported modes within the SMA than are supported within the input MMF.

For a given fibre, a and Θ, the V parameter scales inversely with wavelength (equation 4). At point A in Fig. 4 $V = U_{\max}$ and from equation (7) $\theta_{\max} = \Theta$. At all $\lambda > \lambda_{\min}$ the line $V = U_{\max}$ is accessible and so therefore is the numerical aperture of the fibre. However, for all $\lambda < \lambda_{\min}$ the maximum value of U transmitted by the SMA remains as $U_{\max}$ but V still scales inversely with λ and again by equation (7) then $\theta_{\max}$ also becomes inversely proportional to λ. In other words, the maximum input ray angle accepted by the fibre becomes wavelength dependent. The on-sky consequences of this effect are discussed in Sections 4 and 5.

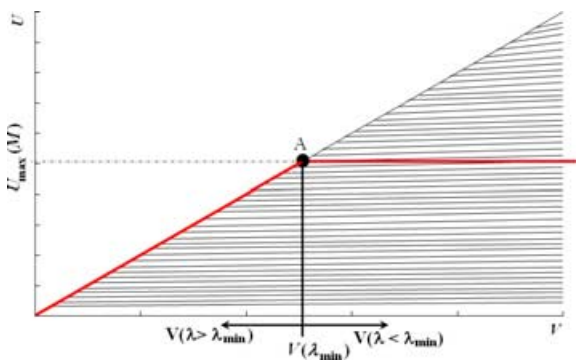

Figure 4. Toy model plot of the MMF U (V) showing $U_{\max}$ associated with the M modes supported within the SMA.

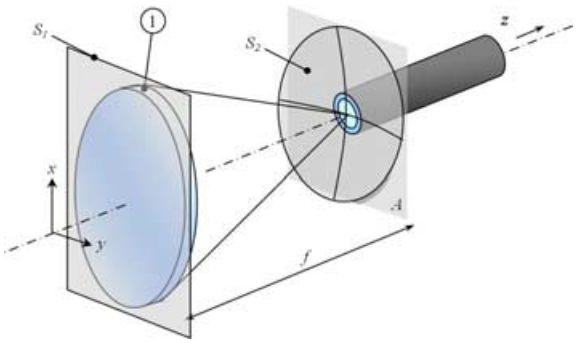

Figure 5. The generalized optical model used in this analysis. The field S_1 is incident on optical element (1) that is monolithic in the x–y plane and is characterized by some positive value of optical power and a limiting, diffracting aperture assumed to be circular. S_1 passes through the lens and is then allowed to propagate the distance f, to the parabolic image surface, S_2. A is the infinite plane containing the fibre end-face. A and S_2 are coincident at the z-axis.

3 THE COUPLING MODEL

Even though the geometrical model is applicable in this analysis, we need to use the full electromagnetic coupling model to examine the applicability of the ray optical model in the diffraction limit and thence to explain how the MPDs are altered under conditions of natural seeing. With reference to Fig. 5, the Cartesian triplet (x, y, z) is orientated such that the fibre and optical axes are co-aligned with z. The coupling efficiency, ρ_n, of the field $\boldsymbol{E}_i$, in the infinite transverse plane, A, that contains the input end-face of the fibre, into the modal field $\boldsymbol{h}_{x,y}$ of the fibre is given by

$$\rho_n = \frac{\left(\int_A \mathrm{d}A\, \boldsymbol{E}_i \times \boldsymbol{h}^*_{x,y} \cdot \hat{\boldsymbol{m}}\right)^2}{\mathrm{Re}\left[\left(\int_A \mathrm{d}A\, \boldsymbol{E}_i \times \boldsymbol{H}^*_i \cdot \hat{\boldsymbol{m}}\right)\left(\int_A \mathrm{d}A\, \boldsymbol{e}_{x,y} \times \boldsymbol{h}^*_{x,y} \cdot \hat{\boldsymbol{m}}\right)\right]}, \tag{9}$$

where $\hat{\boldsymbol{m}}$ is the unit vector in the z-direction and the subscript. In the weakly guiding regime, the z-component of even the HE and EH modal fields is negligible by comparison to $\boldsymbol{h}_{x,y}$, hence equation (9) is a good estimate of the coupled power with the total guided power, ρ_{T}, within a fibre supporting N modes given by

$$\rho_{\mathrm{T}} = \sum_{i=1} \rho_i. \tag{10}$$

For $U \gg 1$ the modes of the MMF asymptotically approach a set of plane waves of discrete angular spectrum (Snyder & Love 1983) as illustrated in Fig. 3(a), and equation (7) and so equation (10) should be recognized as yielding the magnitudes of a Fourier-like series decomposition of $\boldsymbol{E}_i$. This likeness has a significant impact on the MPDs for various $\boldsymbol{E}_i$.

3.1 The input field designation

Assuming that all optics in this analysis are slower than $f/1.5$ allows the use of scalar field optics with negligible vectorial effects, such as coupling between orthogonal field components for instance, due to highly polarized light (Born & Wolf 2003). The modes of the fibre are described vectorially; however, choosing $\boldsymbol{E}_i$ to be polarized in the x-direction yields no loss of generality because the fibre cross-section is assumed circularly symmetric. With reference to Fig. 5, in astronomy either the fibre is generally fed directly with the telescope PSF or a lenslet is placed in a telecentric image plane so that an image identical to the telescope entrance pupil is placed

on the fibre end-face. In the direct feed case, optical element 1 is the telescope itself and f is generally so large that the quadratic surface, S_2, is approximately planar over any area, A, of interest. If S_1 is an unaberrated plane wave then an Airy pattern (Born & Wolf 2003) appears in S_2, such that

$$E_{xi}(x, y) = \frac{J_1\left(\frac{k|\boldsymbol{r}|}{2F_T}\right)}{\left(\frac{k|\boldsymbol{r}|}{2F_T}\right)} - \varepsilon^2 \frac{J_1\left(\frac{\varepsilon k|\boldsymbol{r}|}{2F_T}\right)}{\left(\frac{\varepsilon k|\boldsymbol{r}|}{2F_T}\right)}, \tag{11}$$

where E_{xi} is the x-component of the input field in A, $\boldsymbol{r} = (x, y)$ and F_T is the feed focal ratio into the plane of A. k is the local wavenumber at the fibre end-face and ε is the obscuration due to the telescope secondary (not shown) such that $\varepsilon \in [0.00, 1.00]$.

In the lenslet feed case, the PSF of the telescope resides in S_1 and a Fourier relationship between S_1 and S_2 exists (Goodman 1996). The telescope PSF in S_1 is vignetted by the aperture of the lenslet and this effect causes diffractive features to appear in the telescope pupil image on the fibre end-face (see Fig. 11a). Further, by the convolution theorem, since S_1 is the multiplication of the telescope PSF and the pupil function of the lenslet then S_2 can be taken as the convolution of the telescope pupil image and the PSF of the lenslet. Projecting S_2 on to A then yields a multiplicative spherical term and the pupil image is taken as

$$E_{xi}(x, y) = \exp\left[\mathrm{i}\frac{k_o}{2f_l}(x^2 + y^2)\right] h \otimes E_{xg}, \tag{12}$$

where E_{xg} is the x-component of the geometrical image of the telescope entrance pupil, $\boldsymbol{h}$ is the PSF of the lenslet and f_l is the focal length of the lenslet.

The modal and incident fields were computed on a 1000^2 grid; however, by inspection, some of the higher order modes required a larger matrix and these were increased in size in order that the smallest feature within the modal distribution was at least Nyquist sampled and in most cases considerably better than this. A simple mid-point integration routine was found to produce the most stable results in comparison to analytical solutions. We chose to model numerically instead of searching for analytical solutions since no general solution is likely to exist for the case of the diffracted pupil image without significant approximation and certainly no solution is likely for the case of the atmospherically aberrated telescope PSF.

4 AIRY PATTERN COUPLING

4.1 Ideal seeing

In this section we compare the predictions of the ray geometrical and the electromagnetic coupling models when the fibre is fed directly in the telescope image plane (see Fig. 6).

We first define the V parameter in terms of the Rayleigh length, w, of the unaberrated telescope PSF which in the scalar optical approximation is given by

$$w = 1.22 F_T \lambda. \tag{13}$$

This is the 1/2 width of the diffraction limited Airy pattern out to the first zero in electric, or therefore first minimum in intensity. Rearranging equation (13) for λ and substituting into equation (4) yields

$$V = \frac{2.44\pi\Theta\ F_T}{(w/a)} \tag{14}$$

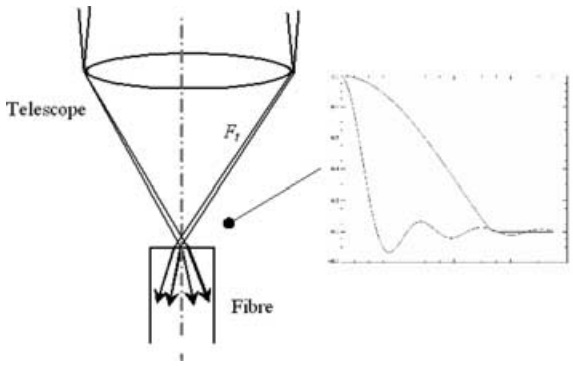

Figure 6. The geometrical ray model and inset the Airy pattern $\Re(E_{xi})$ and fibre fundamental mode for the case of $(w/a) = 0.3$.

which describes the fibre and telescope together. However, equation (4) is a special case of equation (7) and since $\theta = 1/2F_T$ then

$$U_{F_T} = \frac{1.22\pi}{(w/a)}, \tag{15}$$

where U_{F_T} describes the part of the $U(V)$ space occupied by the feed of focal ratio F_T from the telescope.

Figs 7(a)–(c) are the MPDs of an Airy pattern coupling into the fibre at $(w/a) = 0.1$ when the PSF is the on-the-fibre axis, 20 per cent (of the fibre core radius) off-axis and 60 per cent off-axis. The ordinate is expressed as SMA mode number, where $1 = \mathrm{HE}_{11}$, $2 = \mathrm{TE}_{01}$, $3 = \mathrm{HE}_{21}$, $4 = \mathrm{TM}_{01}$ and so on – see Section 2.1 – in order that the number of cores required within the SMA can be immediately read from the figure.

In the electromagnetic coupling case, the Fourier transform of an Airy pattern is a top hat and so the form of the MPD in Figs 7(a)–(c) should not be surprising. As the Airy pattern moves off-axis, the Fourier transform would include a cosine term modulating the electric field with the result that the MPD of the fibre redistributes the available power into more and more modes within the envelope of the top hat as the fractional offset from the fibre axis increases.

Again appealing to the Fourier series analogy and focusing only on the numerical value of (w/a), as this quantity decreases, smaller spatial frequencies in the image field $\boldsymbol{E}_i$ appear which require higher order modes within the fibre to couple into. Fig. 7(d) shows that indeed this is the case. Note the linear population of the cumulative curve as appropriate to a top hat 'modal transform'. The number of modes required to couple the light efficiently is given, from Fig. 7(d), by the fit $M_{\min} = 4.0881\,(w/a)^{-1.9698}$ and substituting this into equation (15) yields

$$M_{\min} \approx \frac{U_{FT}^2}{4}, \tag{16}$$

which shows that the electromagnetic and geometrical coupling models agree well, certainly to within $1/U$.

The case $(w/a) > 0.3$ is not considered because of the increasing loss associated with the vignetting of the PSF by the fibre core. At $(w/a) = 0.3$ the loss is 4 per cent on-axis, although this is much higher in the aberrated case of course – see below. Since $(w/a)_{\max} = 0.3$, from equation (15), $V \approx 13$ is then the minimum value for lossless (on-axis) coupling of an Airy pattern into MMFs. Further, the maximum fractional offset in Fig. 7 is 60 per cent since the coupling efficiency starts to fall off significantly beyond this point for $(w/a) = 0.3$.

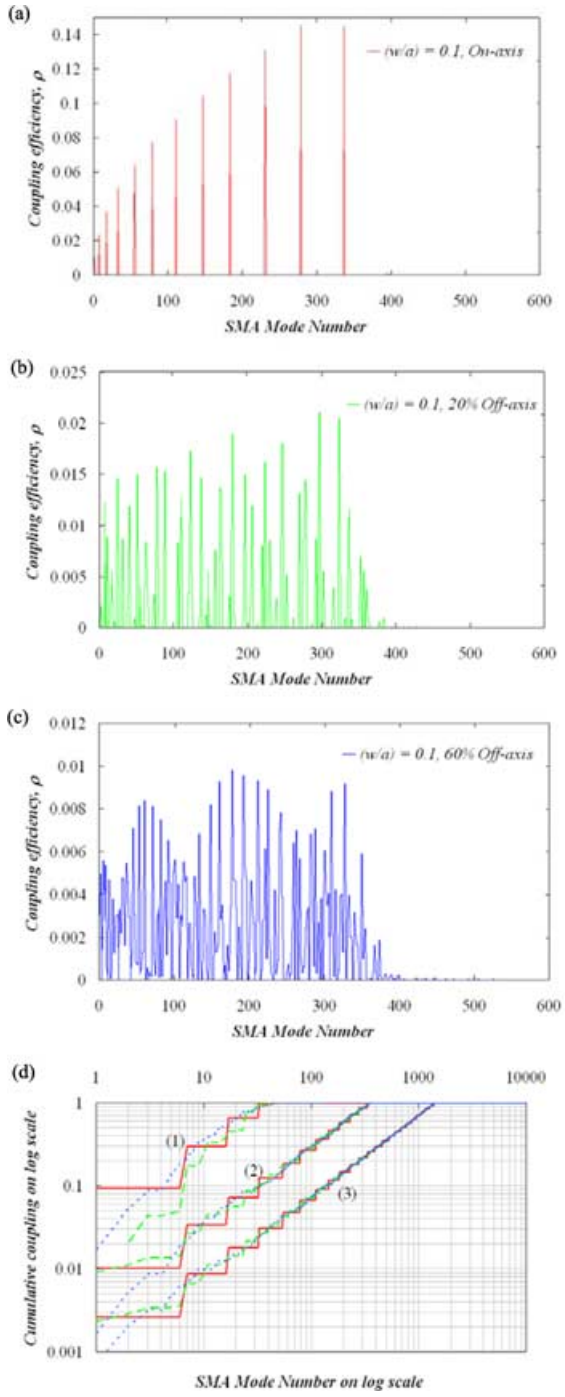

Figure 7. (a)–(c) The MPD of the three cases of on-axis and 20 and 60 per cent off-axis, respectively. (d) The cumulative coupling efficiency, (equation 10) as a function of the SMA mode number when coupling an unaberrated Airy pattern into the fibre on a log–log scale. (*i*) $(w/a) = 0.3$, (*ii*) $(w/a) = 0.1$, (*iii*) $(w/a) = 0.05$. Note that the width of the distribution is a function of (w/a) only (solid line) on-axis, (dashed line) 20 per cent off-axis and (dotted line) 60 per cent off-axis.

4.2 *M*, transmission and field of view

What are equations (15) and (16) actually telling us about how many modes must be supported within the SMA for lossless overall transmission? In this section we investigate the relationship between $(w/a) < 0.3$ and M, the number of SMA modes in the array. From

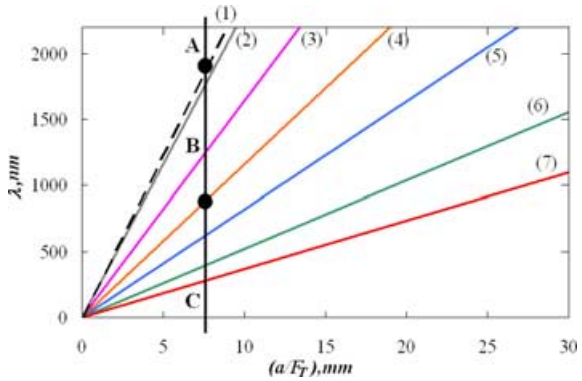

Figure 8. A plot of the wavelength against (a/F_T) for the number of modes supported within the SMA, (1) $M = 45$, (2) $M = 50$, (3) $M = 100$, (4) $M = 200$, (5) $M = 400$, (6) $M = 1000$, (7) $M = 2000$.

equations (4) and (14),

$$\lambda = \left[\frac{(w/a)}{1.22}\right]\left(\frac{a}{F_T}\right). \tag{17}$$

Since the number of modes in the SMA, M, will be limited by manufacturability, we plot the straight lines of λ against (a/F_T) for various $(w/a) = 2/\sqrt{M}$, in Fig. 8, up to the limit of $(w/a) = 0.3 \Rightarrow M = 45$.

The lossless wavelength range accessible by a fibre of $(a/F_T) = 7.5$ is shown as region B along the vertical line in the figure. Wavelengths in region A imply that $(w/a) > 0.3$ which means that the energy of the Airy pattern is vignetted by the fibre core and falls off in a highly non-linear manner, both as λ increases and as the Airy pattern moves about on the fibre end-face. In region C $\lambda < \lambda_{min}$ (Fig. 4) and not enough modes are supported within the SMA to fully transmit all of the energy of the PSF. Note that each of the on-axis through to 60 per cent off-axis cumulative curves in Fig. 7(d) is almost identical at each (w/a) even on the sloped part of the curve relating to the region below the dot on the vertical line in Fig. 8. Hence, when the fibre is operated in region C, the field of view of the MMF on the sky is unaffected by the truncation of the MMF modes by the SMA in the Airy pattern feed case, but the transmitted power is inversely proportional to λ^2 and from equation (17)

$$T_M = (\lambda/\lambda_{min})^2, \quad \text{for } \lambda < \lambda_{min}. \tag{18}$$

An example transmission spectrum, affected by equation (18), is shown for the case of natural seeing in Fig. 10(g) in Section 4.3.

The example in Fig. 8 at $(a/F_T) = 7.5$ μm shows that for simultaneous access to the entire 800–1800 nm range typically associated with OH line emissions, a minimum of 200 modes is required in the diffraction limit. If the shortest desired wavelength, λ_{min}, can be increased, then the number of modes required is also reduced as described by equation (17). However, in the specific cases of *J*- and *H*-band coupling, $M_{1.15\,\mu m} = 57$ modes and $M_{1.49\,\mu m} = 66$.

As a practical example, Leon-Saval et al. (2005) first demonstrated SM performance in an MMF. Their specific example was a 19 SMA mode fibre array device; so if the 200 supported modes from the above example were taken as a reasonable extrapolation and made into a fibre, this would mean $(a/F_T) \approx 7\,\mu m$ and for $F_T = 8$ then $a = 55\,\mu m$, or a 110-μm core diameter fibre.

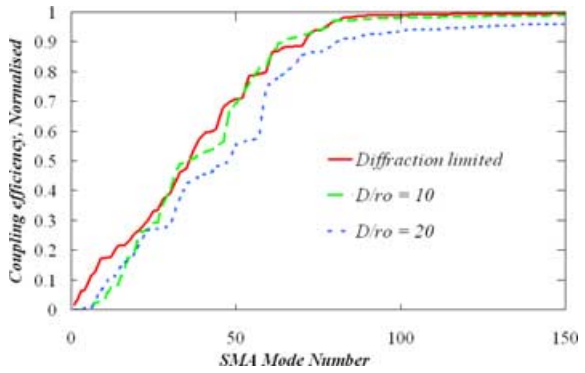

Figure 9. A comparison of the MPDs of the diffraction limited, $D_T/r_o = 10, 20$ cases, where D_T is the telescope primary diameter and r_o is the Fried parameter. D_T/r_o is specified at 500 nm.

4.3 Airy pattern coupling — natural seeing

We now examine the effect, on the MPD, of coupling atmospherically degraded PSFs. From the results of Section 4.1, in designing an OH-suppressing fibre system there is a trade-off between the need to decrease (w/a) to collect more energy and to reduce the number of modes, M, by increasing (w/a) since $(w/a) \propto 1/\sqrt{M}$. Fig. 9 shows that the geometrical model is still applicable even under conditions of natural seeing that yield a speckle pattern in the telescope image plane. The reason for this is that regardless of how badly aberrated the PSF is, it is still the Fourier transform of the telescope exit pupil. Thence, regardless of how poor the seeing might be, the width of the modal transform will always be limited by the limiting aperture of the telescope exit pupil.

Fig. 10 is the same as Fig. 8 but under conditions of natural seeing typically found on 4- and 8-m class telescopes. For each telescope/atmosphere, 1000 PSFs were generated using a Monte Carlo simulation, and for each one the coupling integral was evaluated. The atmosphere was simulated as a randomly generated Kolmogorov phase screen and the PSF was constructed using the far-field approximation [by taking a fast Fourier transform (FFT) of the complex field in the telescope pupil]. Perfect tip-tilt correction of the pupil phase was assumed, and the intensity in the telescope pupil was assumed to be uniform, i.e. scintillation effects were not included.

The amount of AO correction applied is indicated by the number of radial Zernike orders corrected, rz. For instance the 7- and 12-rz cases are high-order corrections as typically found on 4- and 8-m class telescopes, respectively, whereas 1 rz is interpreted as tip-tilt only correction.

The geometrical relationship equation (17) remains valid in conditions of natural seeing, but now the PSF is spread further out in the image plane due to the atmospherically degraded wavefront in the telescope entrance aperture. Therefore only some fraction of the energy in the PSF will couple into the fibre core of radius, a, with the remaining energy incident on the fibre cladding/buffer and therefore not transmitted by the fibre. As noted above, there is a trade-off between the need to minimize (a/F_T) to minimize M and to maximize (a/F_T) to reduce vignetting loss.

4.4 Results

Since a transmission estimate is our goal, the plots in Fig. 10 are of the energy in the aberrated telescope PSF enclosed by the fibre core for (a), (b) 84 per cent in 10- and 15-cm seeing, respectively, (c), (d) 50 per cent in 10- and 15-cm seeing, respectively, and (e), (f) 30 per cent in 10- and 15-cm seeing, respectively. An overall example transmission spectrum is shown in panel (g).

The bold black lines are the n per cent transmission points for λ as a function of (a/F_T). They do not include any contribution from equation (17) and are due only to the vignetting loss of the aberrated telescope PSF on the fibre core. For any given value of (a/F_T), wavelengths above the straight lines on the graph (similar to Fig. 8) do not suffer from losses due to insufficient numbers of modes in the SMA. Below the straight lines, the transmission falls off as a product of the vignetting of the PSF by the core and equation (18) and so for maximized transmission for some given number of modes, wavelengths below the line associated with M (equation 17) should be avoided. The results are therefore interpreted as follows.

4.4.1 84 per cent transmission

Points A and B on panels (a) and (b) show that the upper part of the H band is accessible, at 84 per cent transmission, to the 8-m class telescope in 10 and 15 cm by using $M = 200$ and 400 SMAs, respectively. However, this accessibility is achieved with a significant 12 radial orders of correction from the AO system. The 4-m class telescope easily reaches the lower J band in the $M = 200$ case in the 15-cm case [panel (b), points C and D] even with only tip-tilt correction. However, even the $M = 200$ is likely to be difficult to manufacture, so note that 50–100 modes in the SMA allow access to the upper H band on the 4-m telescope in 15-cm seeing at 84 per cent efficiency.

4.4.2 50 per cent transmission

50 per cent transmission is possible on the 8-m class telescopes, even in 10-cm seeing, with $M = 200$ in the J band with $M = 50$–100 required for the H band. The 4-m class telescope is capable of 50 per cent transmission in the J band with $M = 50$ modes and in the H band with $M \ll 50$ modes.

4.4.3 30 per cent transmission

If the manufacturability of these devices is limited to a few tens of modes, say $M \leqslant 50$ then the 4-m 50 per cent and 4- and 8-m 30 per cent plots are going to be the most relevant, highlighting the direct relationship between the size of the telescope, the number of required modes and resulting transmission.

4.4.4 An example transmission spectrum

Fig. 10(g) shows the theoretical transmission spectrum of an SMA with $M = 200$ cores. That is, the transmission as a function of wavelength for various fixed (a/F_T). The 8-m $(a/F_T) = 7\,\mu$m and 8-m $(a/F_T) = 13\,\mu$m cases highlight that the larger fibre can be used to couple more light in for the same 'size' PSF but by equation (17) this then increases λ_{min} to, in this case, 1500 nm at $(a/F_T) = 13\,\mu$m. For $\lambda < \lambda_{min}$, the transmission then falls off as a product of equation (18) and the vignetting loss.

4.4.5 Direct feed – comment

Any comments made about the applicability of this technology must depend, largely, on the manufacturability of the SMA device. On the basis that 200 modes are difficult but achievable, 50–100 modes

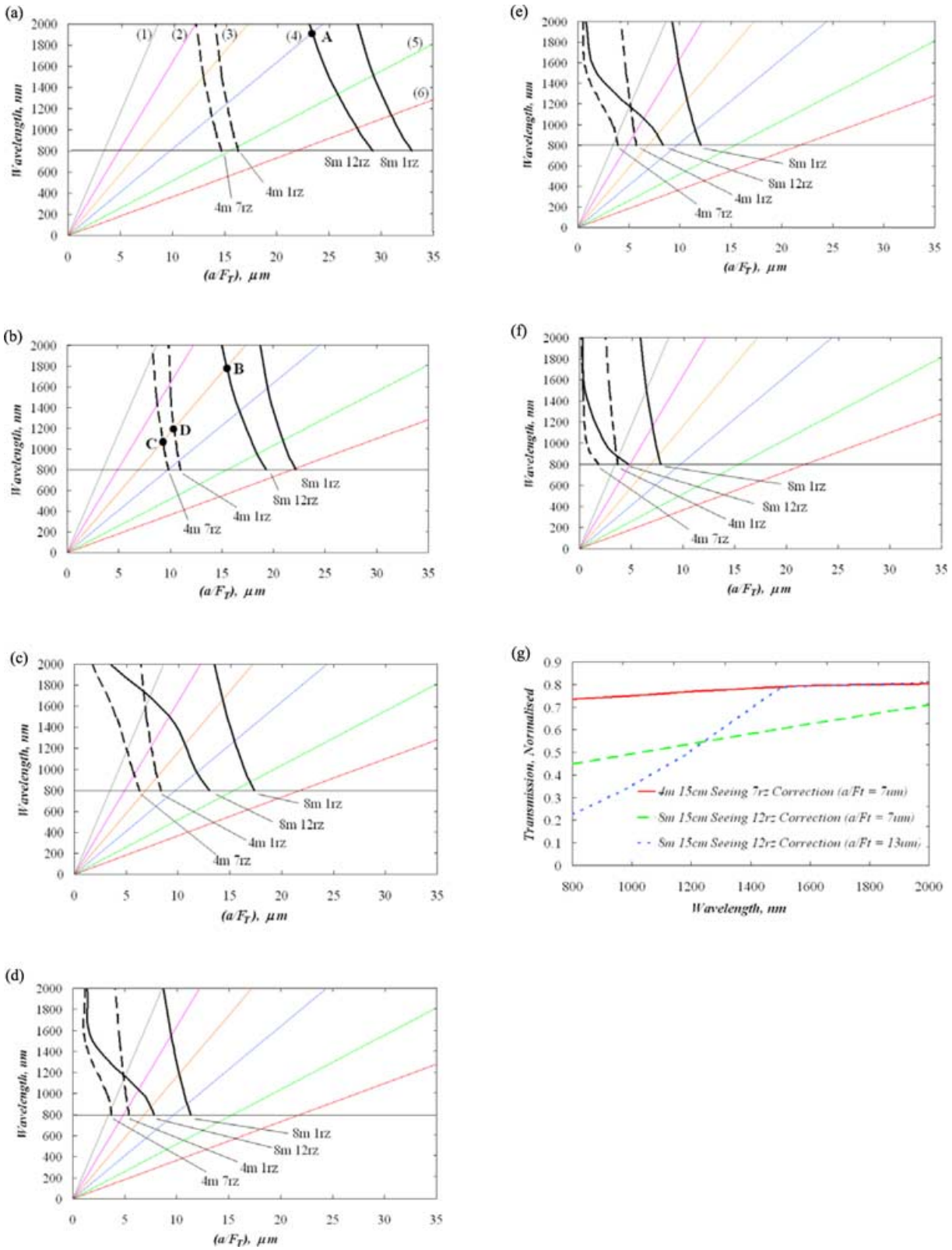

Figure 10. The black lines in this figure represent (a) 84 per cent enclosed energy within the fibre core diameter for $r_o = 10$-cm seeing (specified at 500 nm), (b) 84 per cent enclosed energy within the fibre core diameter for 15-cm seeing, (c) 50 per cent enclosed energy within the fibre core diameter for 10-cm seeing, (d) 50 per cent enclosed energy within the fibre core diameter for 15-cm seeing, (e) 30 per cent enclosed energy within the fibre core diameter 10-cm seeing, (f) 30 per cent enclosed energy within the fibre core diameter for 15-cm seeing. The key is $M = 50$, 100, 200, 400, 1000 and 2000. 1 rz is tip-tilt only corrected and 7 and 12 rz, 7 and 12 radial orders of correction on 4- and 8-m class telescopes, respectively. (g) Typical transmission spectrum of an $M = 200$ fibre.

might eventually be routine, and on the results above note the following (all quoted for 15-cm seeing).

8-m class telescopes. *J*-band transmissions of 50 per cent are achievable with tip-tilt only and 12 radial orders of correction for $M = 200$ and 50 modes in the SMA, respectively [panel (d)]. *J*-band transmissions of >80 are only possible with $M > 200$ modes [panel (b)]. *H*-band transmissions of >50 per cent are possible for the $M = 50$ case and 12 radial orders of correction [panel (c)], but $M = 200$ and 12 radial orders of correction are required for >80 per cent transmission [panel (b)].

4-m class telescopes. *J*-band transmissions of >84 per cent are achievable with $M = 100$–200 modes, even with only tip-tilt correction [panel (b)]. Greater than 84 per cent is achievable in *H* band with only $M = 50$–100 modes in the SMA [panel (b)].

Therefore it would seem that whilst the technology is in its infancy, it is rather more applicable to 4-m class (or less) telescopes than Very Large Telescopes when illuminated directly in the telescope image plane. However, as we learn more about how to manufacture these devices, this may change in future.

5 PUPIL COUPLING

5.1 Negligible spherical term – ideal seeing

Fibre-based integral field spectrographs generally feed an array of fibres with a lenslet array contiguous in the telescope image plane. If OH-suppressing fibres can be made cheaply enough, they might also find use in this application. The lenslet places an image of the telescope exit pupil on the end-face of the fibre, and in this section we investigate the properties of OH-suppressing fibres when illuminated in this way.

In the first instance, we will ignore any effects due to the projection of S_2 on to A and assume that the spherical term is negligible to further demonstrate the relationship between the electromagnetic and ray optical models. This leads on naturally to the more general case where the spherical term is not negligible.

Fig. 11 again highlights the decomposition relationship between the MPD and $\boldsymbol{E}_i$ since the 'modal transform' of the pupil function appears to very similar to an Airy pattern. Indeed, by increasing the telescope secondary mirror obscuration of its exit pupil, the well-known reinforcement of the first Airy minima occurs as λ increases (Linfoot & Wolf 1952). Here the fibre is illuminated with pupil images of an infinitely distant point sources at various equally spaced points from on-axis to the furthest possible physical extent, in this case the numerical aperture of the fibre at 0.22. The geometrical image $E_{\rm xg}$ is then given by

$$E_{\rm xg} = P \exp(\mathrm{i}knx\theta) \tag{19}$$

for pupil function P which takes the value unity within the extent of the pupil image and zero otherwise. As θ, the angle subtended between the line of sight of the object and the fibre axis at the fibre end-face, increases up to the limiting value of the NA of the fibre or the lenslet, whichever is smaller, the tilt in the field increases yielding $\Re\,(E_{\rm xg})$ as shown Figs 12(a)–(c) for instance. The fine, diffractive, detail of the convolution of the pupil image with the lenslet PSF is included in these images. Unless otherwise stated, the lenslet is assumed throughout this analysis to have a focal ratio of *f*/5.

With the Fourier-like model in mind, the mode carrying most power within the fibre is the one whose 'mode angle' (equation 7) best matches θ in equation (19). The broadening of MPD into an Airy pattern occurs because of diffraction, in the sense that the MPD is the modal transform of the image of the exit pupil of the telescope – an Airy pattern.

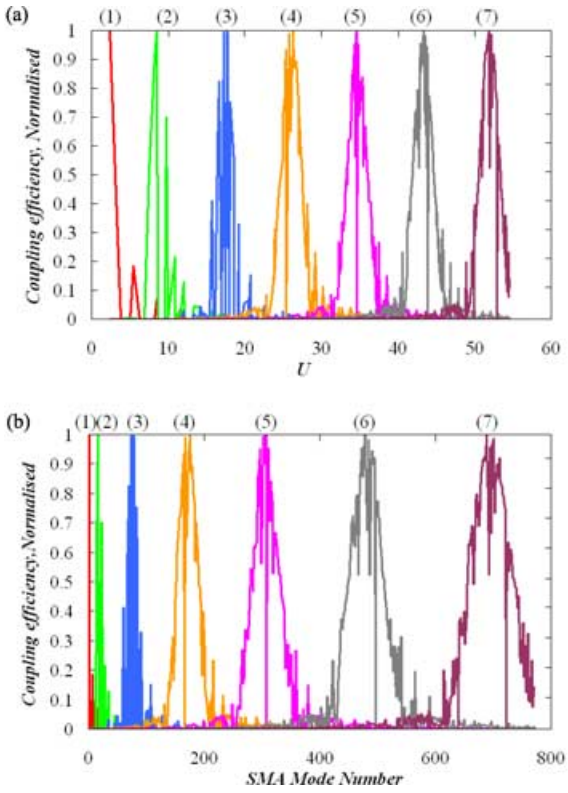

Figure 11. (a) The variation in MPD as a function of U, as the source moves off-axis. (b) The variation in MPD as a function of the number of SMA modes, as the source moves off-axis (1) on-axis, (2) 2°, (3) 4°, (4) 6°, (5) 8°, (6) 10°, (7) 12°.

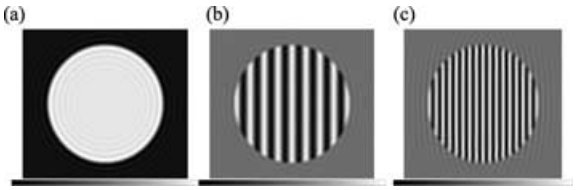

Figure 12. Images of $\Re(E_{\rm xg})$: (a) on-axis, (b) 6° input at fibre end-face, (c) 12° input at fibre end-face; all with no spherical term.

5.2 Non-negligible spherical term – ideal seeing

We now turn to the more realistic case, where the spherical image term (equation 12) is not negligible. Fig. 13(a) shows the MPD associated with a 6° angle of incidence at the fibre, for a $\Theta = 0.22$, 50 μm diameter core fibre fed with three different values of $f_{\rm l}$, the focal length of the field lenslet. The increased angular distribution of light associated with the projection of S_2 on to A causes the MPD to be smeared out about the position of the Airy in the MPD in the non-spherical case. Figs 13(b) and (c) are examples showing the significant extra width associated with even a value of $a/f_{\rm l}$ as low as 0.05.

Geometrically we can think of the extra angular component as being due to the increased angle of incidence of rays associated with the projection of S_2 on to A as shown in Fig. 14.

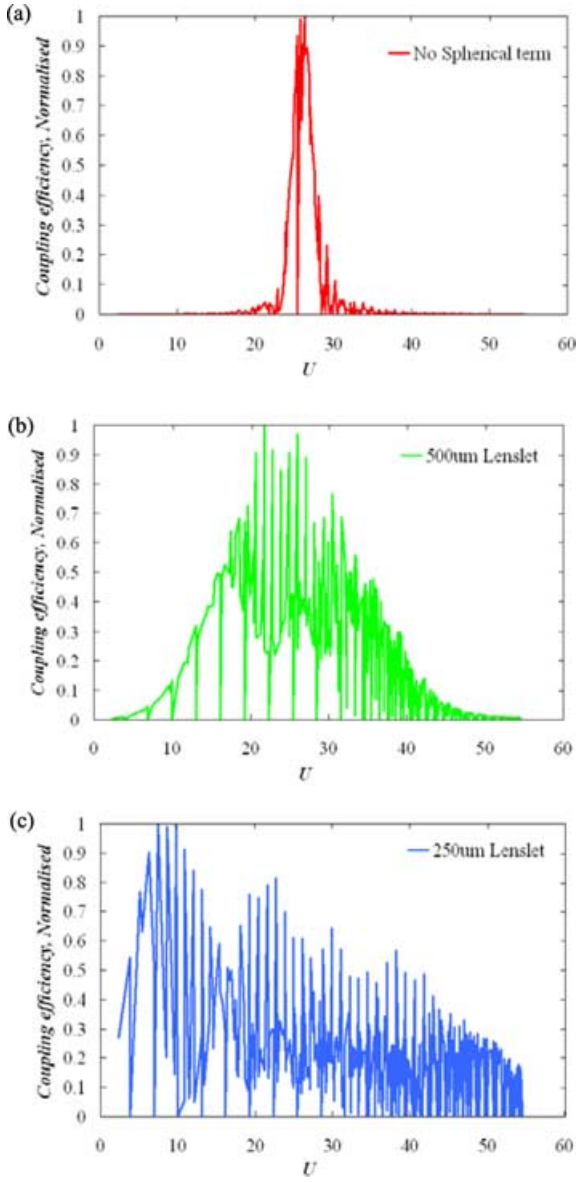

Figure 13. 50-μm fibre core ($a = 25$ μm) fed with (a) no spherical term, (b) $f_{\rm lenslet} = 500$ μm, (c) $f_{\rm lenslet} = 250$ μm.

The increased angular range in A due to the curvature of S_2 is given by

$$\theta \approx \frac{a}{f_1}. \tag{20}$$

This effect is more commonly known as secondary FRD (focal ratio degradation), and the increased range of input angles greater

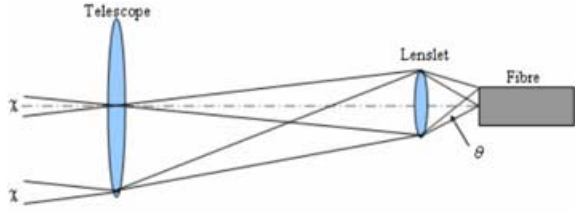

Figure 14. The secondary FRD model. χ is the sample size on the sky.

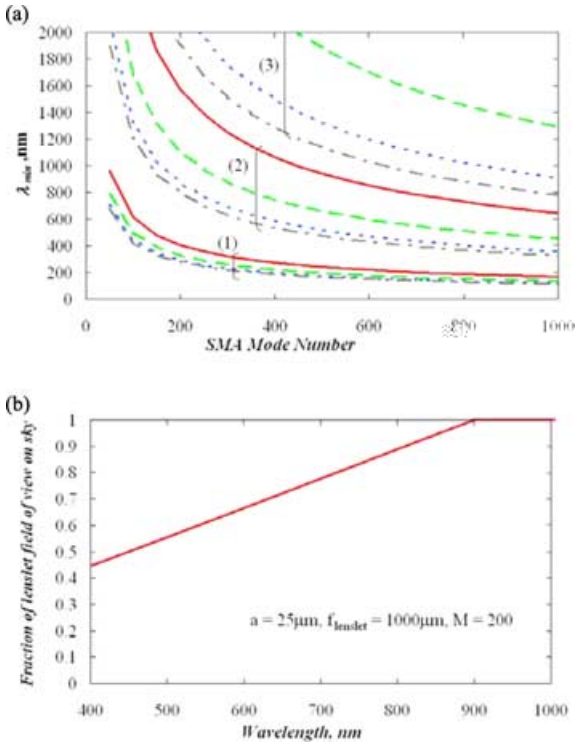

Figure 15. (a) The minimum wavelength that guarantees a wavelength-independent field of view for the case of $F_l = 7.25$, in $n_1 = 1.45$ typically used to avoid FRD issues, (*i*) $a = 10$ μm, (*ii*) $a = 25$ μm, (*iii*) $a = 50$ μm, (dot–dashed) $f_1 = 1500$ μm, (dots only) $f_1 = 1000$ μm, (dashes only) $f_1 = 500$ μm, (solid) $f_1 = 250$ μm. (b) The fraction of the on-sky field of view as a function of wavelength for the case of $a = 25$ μm, $f_1 = 1000$ μm and $M = 200$.

than the focal ratio of the feeding lenslet needs to be allowed for in deriving the relationship between $\lambda_{\rm min}$ and M in the lenslet-fed case.

5.3 The field of view as a function of *M*

In this section we derive a relationship between the field of view of the fibre as a function of M, the number of modes within the SMA. From the previous section, the MPD is directly related to the image of the telescope PSF and so implicit in Figs 11 and 13 was that the telescope PSF was badly undersampled – i.e. the entire telescope PSF passes through the lenslet and is therefore fully visible in the MPD. Generally the size of the lenslets in the telescope image plane would match, at least, the Nyquist sampling criteria of 2 pixels per resolution element. Therefore only some fraction, roughly half for critical sampling, of the telescope PSF would couple into the fibre. However, the aperture function of the lenslet in the telescope image plane forms the maximum extent of the telescope PSF coupled into the fibre, regardless of how badly it might be aberrated by the atmosphere and so the maximum range of angles that couple into the fibre in all atmospheres is given by

$$\theta_{\rm max} = \frac{1}{2F_l} + \frac{a_{\rm image}}{f_1}, \tag{21}$$

where $\theta_{\rm max} < \Theta$, and $a_{\rm image}$ is the radius of the pupil image independent of the core radius. All of the quantities in equation (21) are specified in the region immediately outside the fibre end-face. For example, if the lenslet has a refractive index of n_1, then $F_l = n_1$

$F_{\rm air}$. For $\lambda < \lambda_{\rm min}$, the input ray angle retained by the SMA is given from equations (7) and (8) as, $\theta = (\sqrt{M}\lambda)/(\pi a n_{\rm l})$ where again θ is specified within the feeding lenslet assumed in contact with the fibre end-face. Equating this and equation (21) and rearranging for $\lambda_{\rm min}$, the minimum wavelength at which $\theta_{\rm max}$ is supported within the fibre yields

$$\lambda_{\rm min} = \frac{\pi a n_{\rm l}\left(\frac{1}{2F_l} + \frac{a_{\rm image}}{f_{\rm l}}\right)}{\sqrt{M}}. \quad (22)$$

Fig. 15(a) is a plot of equation (22), where $F_l = 7.25$, $n_{\rm l} = 1.45$ and $a = a_{\rm image}$ and shows that for $M \approx 200$ a wavelength-independent field of view exists for $\lambda_{\rm min} > 800$ nm for only the smallest fibre's core radii, $a < 25\,\mu$m and the largest focal length lenslets, $f_{\rm l} > 1000\,\mu$m. A 100-μm diameter core fibre would require in excess of 250 modes just to access <1600 nm. However, more realistically, referring again to *J*- and *H*-band applications, $M_{\lambda_{\rm min}=1.15\ \mu{\rm m}} = 87$ modes and $M_{\lambda_{\rm min}=1.49\ \mu{\rm m}} = 52$ modes for the case of $a = a_{\rm image} = 25\,\mu$m and $f_{\rm l} = 1000\,\mu$m.

Note also that the practice of undersizing the image with respect to the fibre core usually done to reduce losses from diffractive spreading of the pupil image at higher wavelengths and to avoid centration losses, decreases $\lambda_{\rm min}$ for the same M, or conversely decreases M for the same $\lambda_{\rm min}$. For instance, there is a 10-mode decrease in M if $a_{\rm image}$ is reduced to 90 per cent of a with comparison to the $a_{\rm image} = a_{\rm case}$, when $F_l = 7.25$ and $f_{\rm l} = 1000\,\mu$m for the same $\lambda_{\rm min}$.

Values of a smaller than 25 μm are shown for information in Fig. 15 but are rarely found due to the practical difficulties of lenslet alignment.

Fig. 15(b) shows how the fraction of the on-sky field of view of the truncated fibre changes with λ, for the case of $a = 25\,\mu$m, $f_{\rm l} = 1000\,\mu$m and $M = 200$. Note that if the telescope PSF is well sampled then this reduction in the field of view would, as in the Airy feed case, manifest itself as a reduction in transmission with the square of θ.

5.4 Sampling performance of OH-suppression fibres

We have computed the PSFs of 4- and 8-m telescopes under various conditions of seeing and AO correction, as in Section 4.3. The $a = a_{\rm image} = 25\,\mu$m case was considered as a sensible minimum a for alignment purposes with $F_l = 5$ in air and $f_{\rm l} = 1000\,\mu$m chosen to minimize primary and secondary FRD, respectively. By the conservation of etendue then $F_{\rm T} = 14$ and the size of the lenslet in the telescope image plane is 140 μm.

From Tables 1 and 2, we see that the sampling of the example fibre + feed is rather better matched to the 8-m telescope with near critical sampling of the full width at half-maximum, FWHM, of the PSF in 10-cm seeing and 12 radial orders of correction in the *H* band and in the *J* band for tip-tilt only in $r_0 = 15$cm seeing. The fibre is not well matched to the 4-m telescope with the PSF undersampled even in poor seeing and only tip-tilt corrected.

Since by the conservation of etendue, $F_{\rm T} = (1/2n_{\rm l})(f_{\rm l}/a)$, then increasing $F_{\rm T}$ to better match the sampling of the 4-m telescope would require a decrease in $(a/f_{\rm l})$ which by equation (22) would decrease M due to the decreased secondary FRD (equation 20).

On the 8-m telescope taking $a = a_{\rm image} = 25\,\mu$m and $f_{\rm l} = 1000\,\mu$m, $M = 87$ and 52 modes, respectively, are required to access $\lambda_{\rm min} = 1.15\,\mu$m and $\lambda_{\rm min} = 1.49\,\mu$m (equation 22). To increase $F_{\rm T}$ by a factor of 2 (say) to match the sampling of the 4-m telescope, M thence decreases to 65 and 39 modes, respectively. This can achieved by leaving the fibre core diameter as 50 μm and $f_{\rm l} = 1000\,\mu$m and then reducing the radius of the pupil image (by increasing $F_{\rm T}$) to $a_{\rm image} = 12.5\,\mu$m.

5.5 The effect of defocusing, demagnification and decentration of the pupil image on the MPD

Since an adhesive layer typically exists at the lenslet/fibre boundary, it is common practice to have the focus of the lenslet somewhere just inside the face of the fibre to avoid scattering from defects within the glue. Decentration of the image on the fibre core is also sometimes an issue with the alignment of lenslet arrays with many, potentially very small fibres, a challenging task. However, as we have shown at various points throughout this paper, it is the geometrical ray model that dominates, even when relatively few modes are supported within the MMF. Since the angular range of modes entering the fibre is not affected by either deliberate defocusing or decentring or demagnification of the image with respect to the core size then, to first order, the results of Section 5 are not altered by these effects.

6 SUMMARY

We have presented a simple model of an OH-suppressing fibre as proposed by Bland-Hawthorn et al. (2004) in order to determine how these devices behave on telescope. This general analysis is necessarily presented to an accuracy of $\leqslant$8 per cent due to issues surrounding mode counting near cut-off.

When fed with an Airy pattern, the field of view of the fibre is unaffected by the number of cores/modes in the SMA, M, but the transmission of the device becomes wavelength dependent below some minimum wavelength. The atmosphere was shown to have a significant effect on the performance with the competing needs of reducing M, for manufacturability, whilst increasing the size of the fibre in order to couple more light in from the aberrated telescope PSF. Throughput of greater than 50 per cent was found to be possible at >800 nm on well-corrected (7 rz) 4-m class telescopes for <200 modes at >1500 nm for the same fibre on a 8-m telescope. More realistically, the *J* and *H* bands can be accessed at >80 per cent throughput with <200 and <100 modes, respectively, on the

Table 1. FWHM of the 4-m telescope PSF in various atmospheres and degrees of correction.

4-m telescope Wavelength (nm)	10 cm 1 rz FWHM (μm)	10 cm 7 rz FWHM (μm)	15 cm 1 rz FWHM (μm)	15 cm 7 rz FWHM (μm)
800	235	176	151	104
1000	218.5	156	143	92
1500	194.5	113.5	126	32.3
2000	179	47.5	115	6.4

Table 2. FWHM of the 8-m telescope PSF in various atmospheres and degrees of correction.

8-m telescope Wavelength (nm)	10 cm 1 rz FWHM (μm)	10 cm 12 rz FWHM (μm)	15 cm 1 rz FWHM (μm)	15 cm 12 rz FWHM (μm)
800	486	370	318	219
1000	459	322	299	190
1500	411	258	267	52.5
2000	378	98	243	39.2

well-corrected (7 rz) 4-m class telescope in 15-cm seeing but this reduces to 50 per cent coupling for the same fibre on the 8-m class in the same seeing.

In the pupil-fed case, and assuming that the PSF is well sampled by the feeding lenslet, the field of view of the fibre was shown to become wavelength dependent, again below some minimum wavelength. In this case, the natural scales associated with fibres supporting 50–80 modes were found to match the sampling requirements of the 8-m telescope in the *J* and *H* bands with 40–65 modes for the 4-m telescope. The 4-m case, however, was associated with very small image/fibre scales. Whether or not OH-suppressing fibres find use in IFS will depend largely on how easy (and therefore cheaply) they can be manufactured in bulk.

ACKNOWLEDGMENTS

Many thanks to PPARC for funding this research and to Tim Birks for his invaluable insight. We also had useful discussions with Anthony Horton and Roger Haynes from the AAO and Graham Murray at the CfAI.

REFERENCES

Bland-Hawthorn J., Englund M., Edvell G., 2004, Opt. Exp., 12, 902
Born M., Wolf E., 2003, Principles of Optics. Cambridge Univ. Press, Cambridge
Goodman J., 1996, An Introduction to Fourier Optics. McGraw-Hill, New York
Leon-Saval S., Birks T., Bland-Hawthorn J., Englund M., 2005, Opt. Lett., 30, 2545
Linfoot E., Wolf E., 1952, Proc. Phys. Soc., LXVI, I-B
Pask C., Snyder A., Mitchell D., 1975, J. Opt. Soc. Am., 65, 356
Snyder A. W., Love J. D., 1983, Optical Waveguide Theory. Chapman & Hall, New York

This paper has been typeset from a TEX/LATEX file prepared by the author.